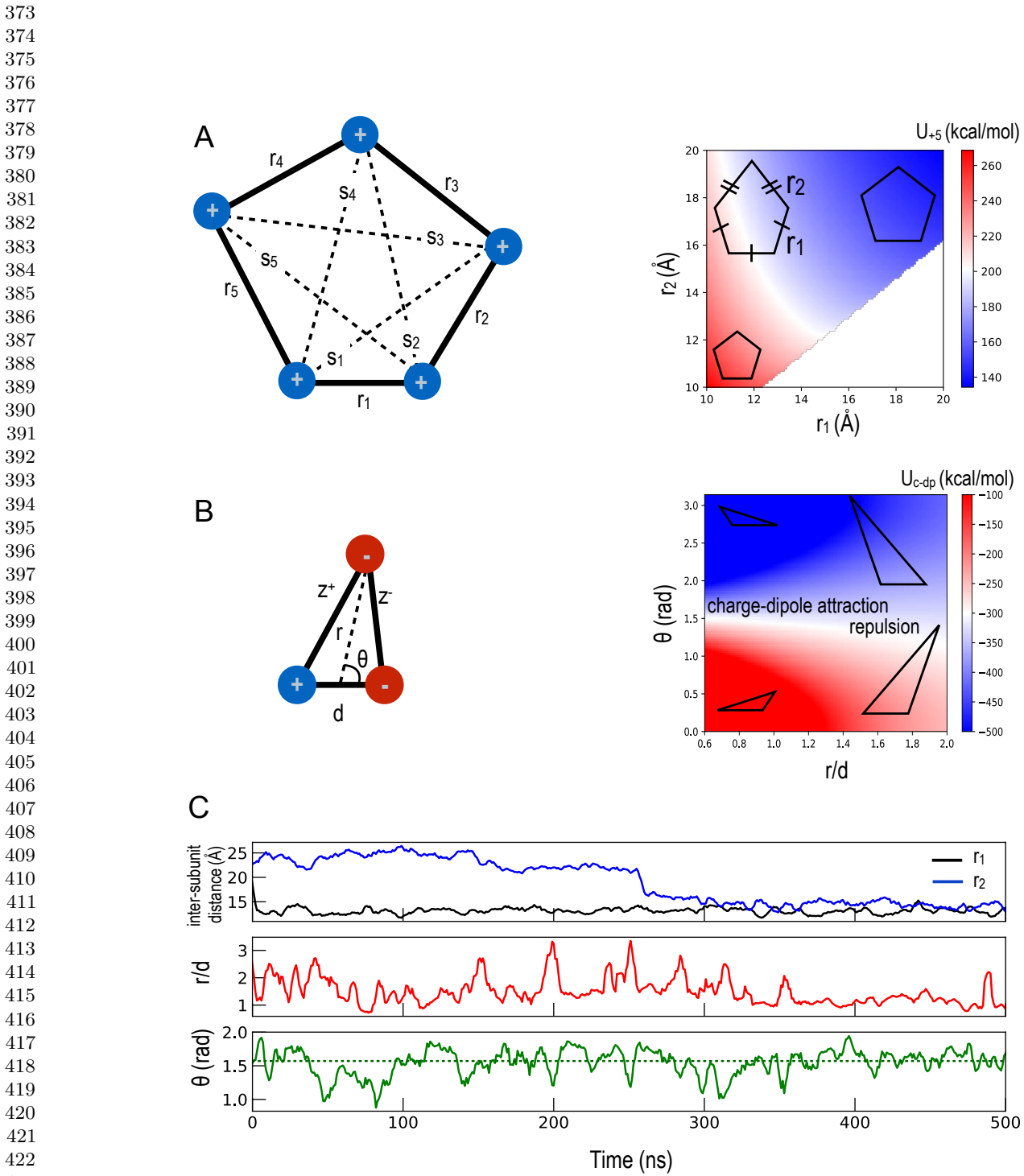


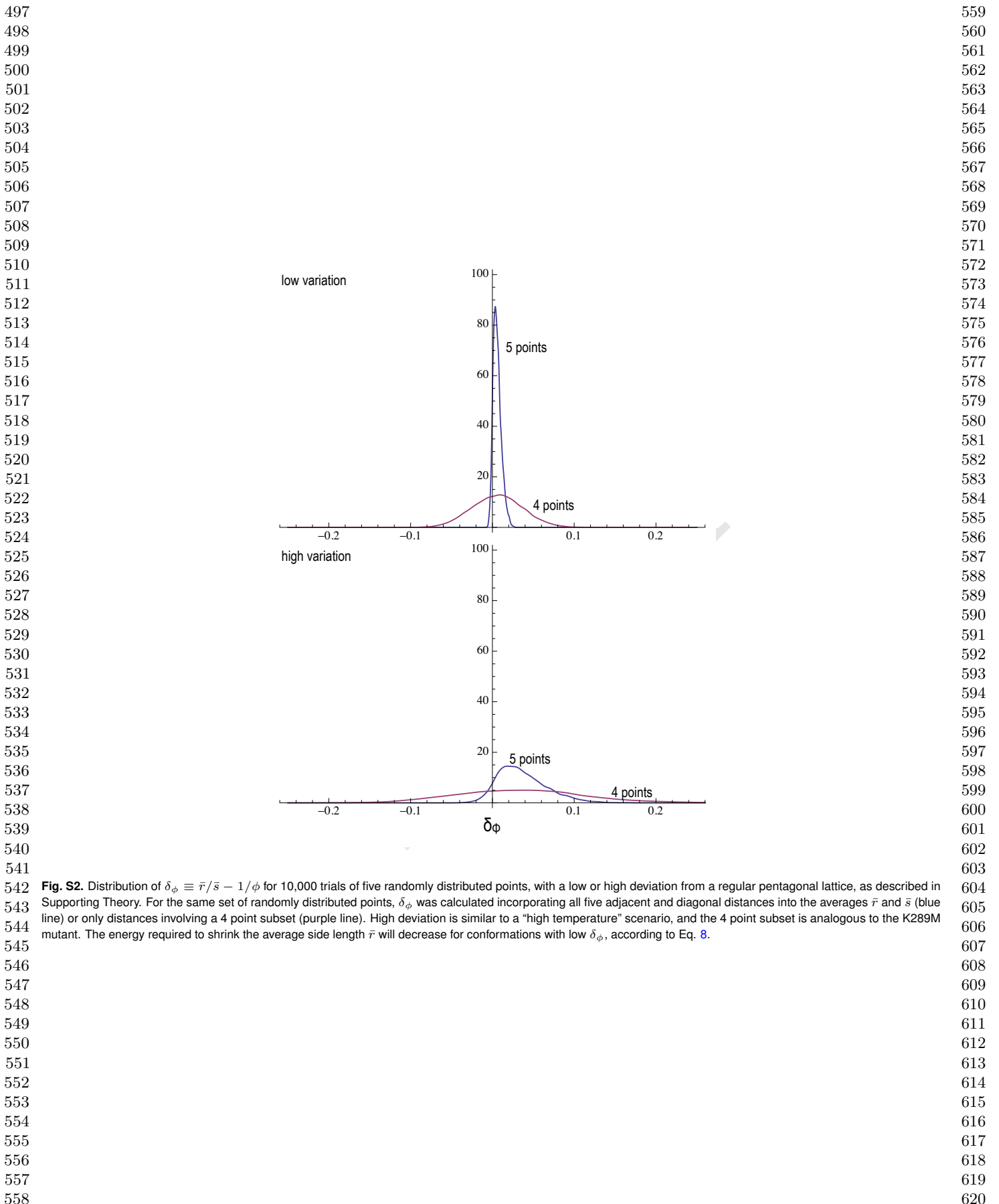
1	<b>Supporting Methods</b>	63
2	The systems were solvated using the SOLVATE plugin in VMD(1) and neutralizing ions were added to bring the system to a	64
3	0.15M salt concentration using the AUTOIONIZE plugin. The final system contained about 160,000 atoms. MUTATE plugin	65
4	was used to introduce the K289M mutation in the $\gamma$ subunit of GABA <sub>A</sub> R receptor.	66
5	All bonds to the hydrogen atoms were constrained using the SHAKE/RATTLE algorithm. A multiple time-step rRESPA	67
6	method was used, and controlled with a high frequency time-step of 2fs and low frequency time-step of 4fs. All the systems	68
7	were energy minimized for 10000 steps, then simulated for 5 ns with restraints of 1 kcal/mol/Å applied to the C <sub>α</sub> atoms of the	69
8	protein. Restraints were then removed and 495 ns of nearly unrestrained simulation was carried out in all four systems at	70
9	low temperature. During this period of the simulation, only harmonic restraints (force constant 0.4 kcal/mol/Å) between the	71
10	intracellular ends of the M3 and M4 helices were used, to mimic the effects of the intracellular domain and prevent separation	72
11	of the M4 helix from the rest of the bundle.	73
12		74
13	<b>Long-range electrostatics.</b> The simulations here used the prescribed cutoff value of 12 Å for the CHARMM forcefield, with a	75
14	switching function past 10Å, combined with PME and a grid size of about 1Å. The distances between charged residues in	76
15	the interfacial band are similar to this cutoff distance, and it is not uncommon to use cutoffs less than 10Å(as in (2)). This	77
16	may cause a significant accumulated error in simulations of any proteins with repeated interactions near the cutoff/switching	78
17	distance, not just pLGICs. In pLGICs, it can reduce the energetic cost of shrinking the interfacial band, leading to an increased	79
18	likelihood of closed states even in WT systems. By recalculating energies using direct Coulomb electrostatics just for interfacial	80
19	band and pore oscillator residues, from a trajectory generated using PME, we found PME reduced the energetic difference	81
20	between elongated and regular conformations by about 5 kcal/mol.	82
21		83
22	<b>SMD Simulations.</b> Steered Molecular Dynamics (SMD) simulations (3, 4) were used to obtain favorable positions of the ion at	84
23	different positions along the channel, for later use in Adaptive Biasing Force (ABF) calculations. The chloride ion was pulled	85
24	along the pore of the channel at a constant velocity of 10Å/ns. The force required to pull at constant velocity is also calculated,	86
25	and can, in principle, be used to calculate a potential of mean force (PMF) using Jarzynski's equation (5, 6), but in practice it	87
26	is challenging to achieve a sufficiently slow pulling speed.	88
27		89
28	<b>ABF Simulations.</b> Adaptive biasing force calculations (ABF)(7–10) were used to measure the potential of mean force (PMF) of	90
29	a chloride ion translocating the GABA <sub>A</sub> R ion channel at 315K, for both the WT and K289M channels. ABF was performed	91
30	using the Collective Variables module(11) of NAMD2.9. The pore axis was divided into 23 bins of each 5Å length.	92
31	Initial coordinates for the ion were obtained from SMD simulations (as described in SI). One thousand samples were collected	93
32	in each bin prior to the application of ABF to avoid undesired non-equilibrium effects on the dynamics. Fifteen ns of trajectory	94
33	were generated in most bins, while bins near the primary barrier in the pore contained 25 ns.	95
34		96
35	<b>Pore Analysis.</b> Measurement and analysis of the pore radii has been carried out using the HOLE software (12) and TCL	97
36	scripting through VMD(1). Python scripts have been used to analyze and visualize the hydration of the pore throughout the	98
37	simulation.	99
38		100
39	<b>Poisson-Boltzmann Calculations.</b> The Poisson-Boltzmann (PB) profile for conduction of both a Na <sup>+</sup> and Cl <sup>-</sup> through the ion	101
40	channel was calculated using APBSmem(13). The pre-generated PQR format of the proteins using PDB2PQR(14) tool was	102
41	used as the input for the electrostatic potential calculations.	103
42	These calculations were performed for initial non-equilibrated structures of the protein, as well as for conformations extracted	104
43	from the last 50 ns of both the 300K and 315K MD simulations (for Cl <sup>-</sup> ).	105
44		106
45	<b>Graphs and images.</b> All plots were calculated and drawn using Python and Tcl scripts. In Figure 2 and the similar supplementary	107
46	figures S5-S11, the series of curves depicting the pore-opening events were further smoothed using a digital filter(Butterworth)	108
47	with a order of the filter value, 2, and a critical frequency value, 0.02, as implemented in the SciPy python module. The time	109
48	derivative of the minimum pore radius was calculated using the gradient function implemented in the numpy python module.	110
49	VMD(1) was used for visualization and for creating molecular images and movies.	111
50		112
51	<b>Supporting Theory</b>	113
52	We consider an irregular pentagon with five side lengths $r_i$ and five diagonal lengths $s_i$ (Figure S1A). The total Coulomb	114
53	energy for the charged ring is given by	115
54		116
55	$U_{+5} = k_e e^2 \sum_i^5 \frac{1}{r_i} + \sum_i^5 \frac{1}{s_i}$	[1]
56		117
57	where $e$ is the electron charge, $k_e = 332\text{Å}/\text{kcal/mol}/e^2$ is the Coulomb constant. Writing each distance as a perturbation from	118
58	the average : $r_i = \bar{r}(1 + \delta r_i)$ and $s_i = \bar{s}(1 + \delta s_i)$ , where the average adjacent length $\bar{r} = \sum_i^5 r_i/5$ and the average diagonal	119
59		120
60		121
61		122
62		123
		124

125 length  $\bar{s} = \sum_i^5 s_i/5$ . Expanding in powers of  $\delta s_i$  and  $\delta r_i$ , 187  
 126  
 127 
$$\sum_j^5 \frac{1}{r_j} = \sum_j^5 \frac{1}{\bar{r}(1 + \delta r_i)} = \frac{1}{\bar{r}} \sum_j^5 (1 - \delta r_i + O(\delta r_j^2))$$
 188  
 128 [2] 189  
 129  
 130  $= \frac{5}{\bar{r}} (1 + O(\bar{\delta r}^2))$  190  
 131 [3] 191  
 132 and similarly, 192  
 133  
 134 
$$\sum_j^5 \frac{1}{s_j} = \frac{5}{\bar{s}} (1 + O(\bar{\delta s}^2))$$
 193  
 135 [4] 194  
 136  
 137 where we have used  $\sum_j^5 \delta s_j = \sum_j^5 \delta r_j = 0$ , and  $\bar{\delta r}^2$  and  $\bar{\delta s}^2$  are the variance in  $r$  and  $s$  across the five sides of the pentagon 195  
 138 respectively. Therefore, 196  
 139  
 140 
$$U_{+5} = k_e e^2 \left( \sum_i^5 \frac{1}{r_i} \right) \left( 1 + \frac{\sum_j^5 \frac{1}{s_j}}{\sum_j^5 \frac{1}{r_j}} \right)$$
 197  
 141 [5] 198  
 142  
 143  $= k_e e^2 \left( \frac{5}{\bar{r}} (1 + O(\bar{\delta r}^2)) \right) \left( 1 + \frac{\frac{5}{\bar{s}} (1 + O(\bar{\delta s}^2))}{\frac{5}{\bar{r}} (1 + O(\bar{\delta r}^2))} \right)$  199  
 144 [6] 200  
 145  
 146  $= \frac{5k_e e^2}{\bar{r}} \left( 1 + \frac{\bar{r}}{\bar{s}} \right) + O(\bar{\delta r}^2) + O(\bar{\delta s}^2)$  201  
 147 [7] 202  
 148  
 149 For a symmetric pentagon  $\bar{s} = \phi \bar{r}$  where  $\phi \equiv (1 + \sqrt{5})/2 \sim 1.62$  is a geometric constant usually called the “golden ratio”, 203  
 150 representing the ratio between the lengths of a pentagon diagonal and side, and with the convenient property  $1/\phi = \phi - 1 = 0.62$ . 204  
 151 We define  $\delta_\phi$  as the deviation of  $\frac{\bar{r}}{\bar{s}}$  from  $1/\phi = \phi - 1 = 0.62$ , so  $\delta_\phi \equiv \frac{\bar{r}}{\bar{s}} - (\phi - 1)$ , and 205  
 152  
 153 
$$U_{+5} = \frac{5k_e e^2 \phi}{\bar{r}} \left( 1 + \frac{\delta_\phi}{\phi} \right) + O(\bar{\delta r}^2) + O(\bar{\delta s}^2)$$
 206  
 154 [8] 207  
 155 The linear term in  $\delta_\phi$  reflects the effects of asymmetry on the relative contributions of diagonal and adjacent distances. 208  
 156 Second-order terms given by  $\bar{\delta r}^2$  and  $\bar{\delta s}^2$  reflect variance in the adjacent and diagonal distances respectively. According to 209  
 157 Eq. 8, positive values of  $\delta_\phi$  (in which diagonal distances are shorter than expected in a regular pentagon) will increase the 210  
 158 overall energy of the interfacial band, provided the average distance between adjacent residues ( $\bar{r}$ ) is kept constant. This 211  
 159 asymmetry-induced increase in energy can be offset by an overall increase in the size of the interfacial band :  $\delta_\phi > 0$  will 212  
 160 stabilize a larger  $\bar{r}$ . Similarly, negative  $\delta_\phi$  will decrease the overall energy of the interfacial band and allow it to decrease the 213  
 161 average separation  $\bar{r}$  with reduced penalty. 214  
 162 Any reduction in  $\delta_\phi$  will thus destabilize the open state. We ran simple numerical calculations to determine how increased 215  
 163 random noise would affect the distribution of  $\delta_\phi$ . Five points were generated with random polar angles corresponding to 216  
 164  $\{0 + \zeta_1, 2\pi/5 + \zeta_2, 4\pi/5 + \zeta_3, 6\pi/5 + \zeta_4, 8\pi/5 + \zeta_5\}$  where  $\zeta_i$  was a random value taken from a flat distribution in the range  $\pm 3\pi/40$  217  
 165 (low variation) or in the range  $\pm 5\pi/40$  (high variation), and the radial values were  $\{1.5 + \rho_1, 1.5 + \rho_2, 1.5 + \rho_3, 1.5 + \rho_4, 1.5 + \rho_5\}$  218  
 166 where  $\rho_i$  was a random value from a flat distribution in the range  $\pm 0.375$  (low variation) or  $\pm 0.625$  (high variation). Although 219  
 167 these are the specific values used in Figure S2 and are given for completeness, the overall trends were not particularly sensitive 220  
 168 to the precise values chosen. 221  
 169  
 170 **S1 Movie:** 222  
 171  
 172 Pore opening event in WT GABA(A) receptor at 315K. View from the extracellular domain showing only the M2 and M3 223  
 173 helices and M2-M3 loop. Charged groups in basic sidechains at M2 24' are shown in blue; orange lines are for visualization 224  
 174 of the interfacial band but do not represent covalent bonds. Charged groups in basic and acidic sidechains at M2 20' are 225  
 175 shown in cyan and red, respectively; white lines are for visualization of the shape of the ‘pore-oscillator’ and do not represent 226  
 176 covalent bonds. Leucine residues at M2 9' forming the hydrophobic gate are shown in gray space-filling representation. A fully 227  
 177 annotated version is in S2 Movie. 228  
 178  
 179 **S2 Movie:** 229  
 180 Fully annotated version of S1 Movie. Pore opening event in WT GABA(A) receptor at 315K. View from the extracellular 230  
 181 domain showing only the M2 and M3 helices and M2-M3 loop. Charged groups in basic sidechains at M2 24' are shown in 231  
 182 blue; orange lines are for visualization of the interfacial band but do not represent covalent bonds. Charged groups in basic 232  
 183 and acidic sidechains at M2 20' are shown in cyan and red, respectively; white lines are for visualization of the shape of the 233  
 184 ‘pore-oscillator’ and do not represent covalent bonds. Leucine residues at M2 9' forming the hydrophobic gate are shown in 234  
 185 gray space-filling representation. 235  
 186

249	<b>S3 Movie:</b>	311
250	Dynamics of the interfacial band, pore oscillator, and hydrophobic gate in K289M GABA(A) receptors at 315K. View from the	312
251	extracellular domain showing only the M2 and M3 helices and M2-M3 loop. Charged groups in basic sidechains at M2 24' are	313
252	shown in blue; orange lines are for visualization of the interfacial band but do not represent covalent bonds. Charged groups in	314
253	basic and acidic sidechains at M2 20' are shown in cyan and red, respectively; white lines are for visualization of the shape of	315
254	the 'pore-oscillator' and do not represent covalent bonds. Leucine residues at M2 9' forming the hydrophobic gate are shown in	316
255	gray space-filling representation.	317
256		318
257		319
258		320
259		321
260		322
261		323
262		324
263		325
264		326
265		327
266		328
267		329
268		330
269		331
270		332
271		333
272		334
273		335
274		336
275		337
276		338
277		339
278		340
279		341
280		342
281		343
282		344
283		345
284		346
285		347
286		348
287		349
288		350
289		351
290		352
291		353
292		354
293		355
294		356
295		357
296		358
297		359
298		360
299		361
300		362
301		363
302		364
303		365
304		366
305		367
306		368
307		369
308		370
309		371
310		372



**Fig. S1.** (A) Adjacent and diagonal distances for the pentagonal Interfacial Band used to calculate averages for Eq. 8, and the associated electrostatic energy for the special case of a pentagon in which three sides are identical and two adjacent sides are also identical, but may differ from the other three. This special case is similar to that observed for the symmetrization step in Figure 2. (B) Definition of terms for the charge-dipole interaction that is formed by three residues in the pore oscillator , as well as associated energy. At around  $\theta = \pi/2$ , the potential energy shifts from decreasing with increasing distance (repulsive) to increasing with increasing distance (attractive). C) Trajectory for defined angles and distances for the K315 replica explored in Figure 2; curves shown here are smoothed much less than in Figure 2 and retain significantly more high frequency noise.



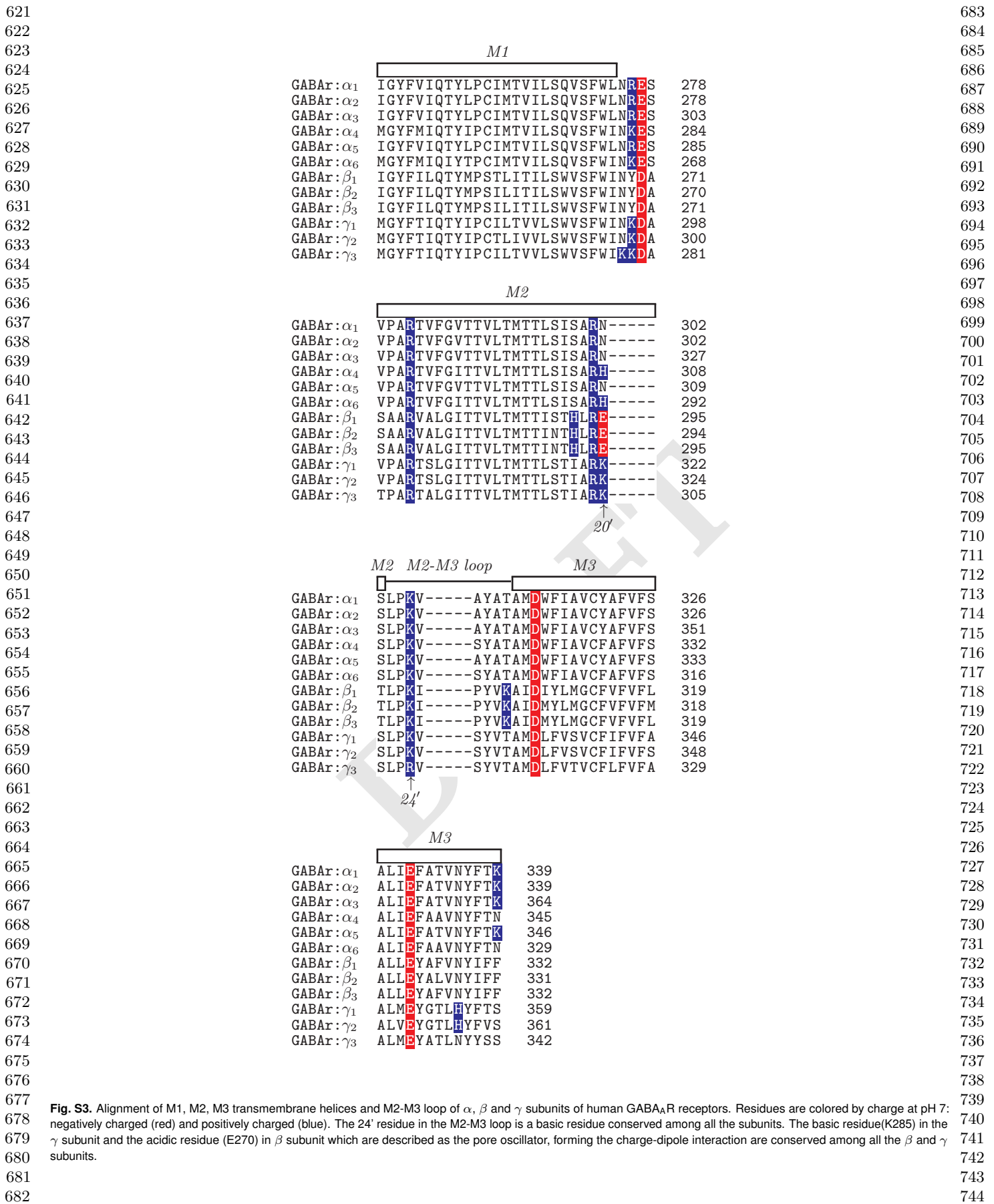
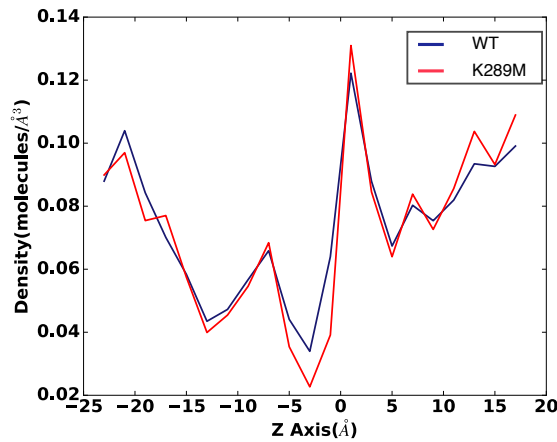


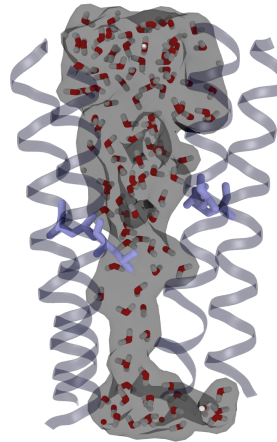
**Fig. S3.** Alignment of M1, M2, M3 transmembrane helices and M2-M3 loop of α, β and γ subunits of human GABA<sub>A</sub>R receptors. Residues are colored by charge at pH 7: negatively charged (red) and positively charged (blue). The 24' residue in the M2-M3 loop is a basic residue conserved among all the subunits. The basic residue(K285) in the γ subunit and the acidic residue (E270) in β subunit which are described as the pore oscillator, forming the charge-dipole interaction are conserved among all the β and γ subunits.

745  
746  
747  
748  
749  
750  
751  
752  
753  
754  
755  
756  
757  
758  
759  
760  
761  
762  
763  
764  
765  
766

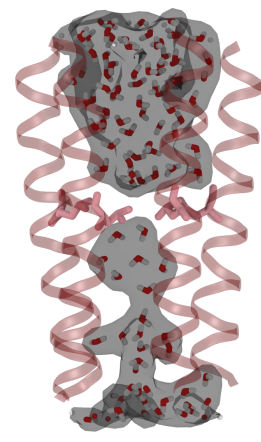
A



B

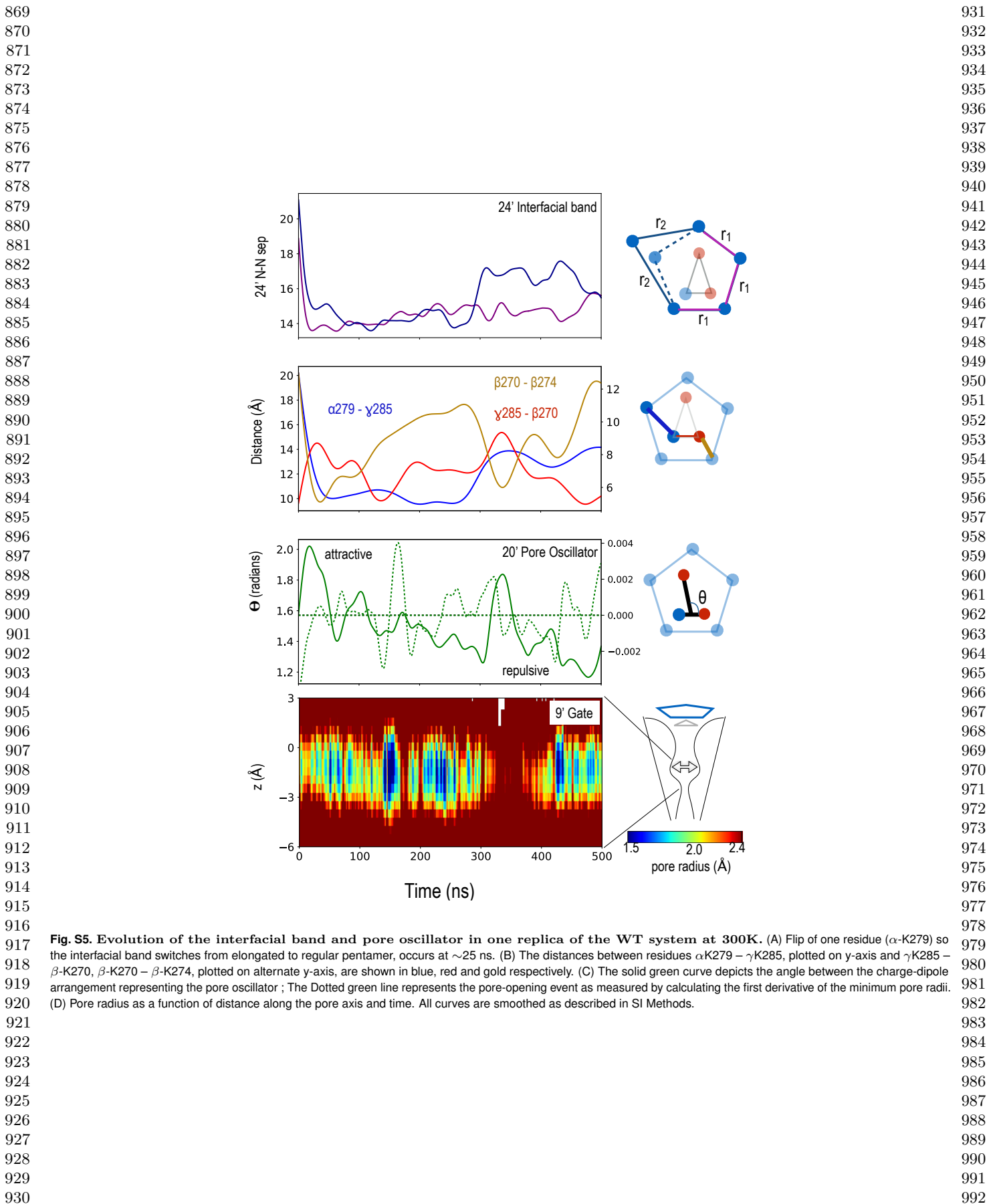


C



783  
784  
785 **Fig. S4.** (A)Number of water molecules along the Z-axis averaged over the frames and replicas. Presence of water in the constriction region of the WT - M2 helices (B) as  
786 compared to the temporary dryness due to reduction in pore radii in the K289M - M2 helices(C), at higher temperature.  
787

807  
808  
809  
810  
811  
812  
813  
814  
815  
816  
817  
818  
819  
820  
821  
822  
823  
824  
825  
826  
827  
828  
829  
830  
831  
832  
833  
834  
835  
836  
837  
838  
839  
840  
841  
842  
843  
844  
845  
846  
847  
848  
849  
850  
851  
852  
853  
854  
855  
856  
857  
858  
859  
860  
861  
862  
863  
864  
865  
866  
867  
868



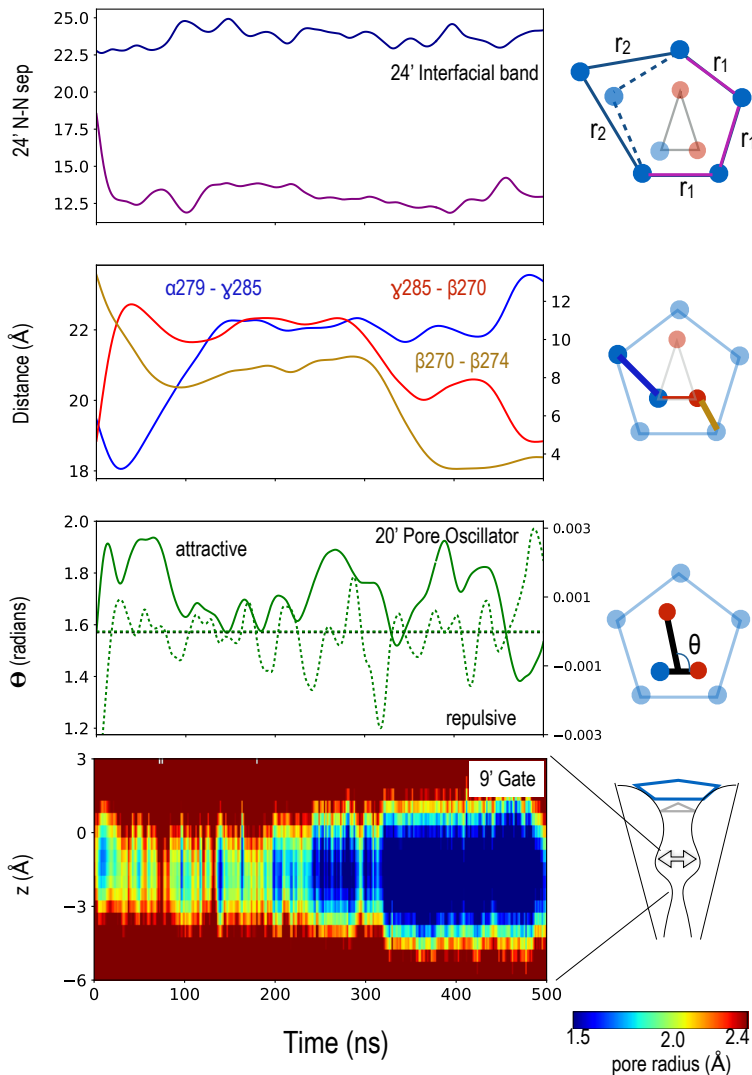


**Fig. S6.** Evolution of the interfacial band and pore oscillator in second replica of the WT system at 300K. (A) Flip of one residue ( $\alpha$ -K279) does not occur and the interfacial band remains in elongated pentamer form. (B) The distances between residues  $\alpha$ K279 –  $\gamma$ K285, plotted on y-axis and  $\gamma$ K285 –  $\beta$ -K270,  $\beta$ -K270 –  $\beta$ -K274, plotted on alternate y-axis, are shown in blue, red and gold respectively. (C) The solid green curve depicts the angle between the charge-dipole arrangement representing the pore oscillator ; The Dotted green line represents the pore-opening event as measured by calculating the first derivative of the minimum pore radii. (D) Pore radius as a function of distance along the pore axis and time. All curves are smoothed as described in SI Methods.

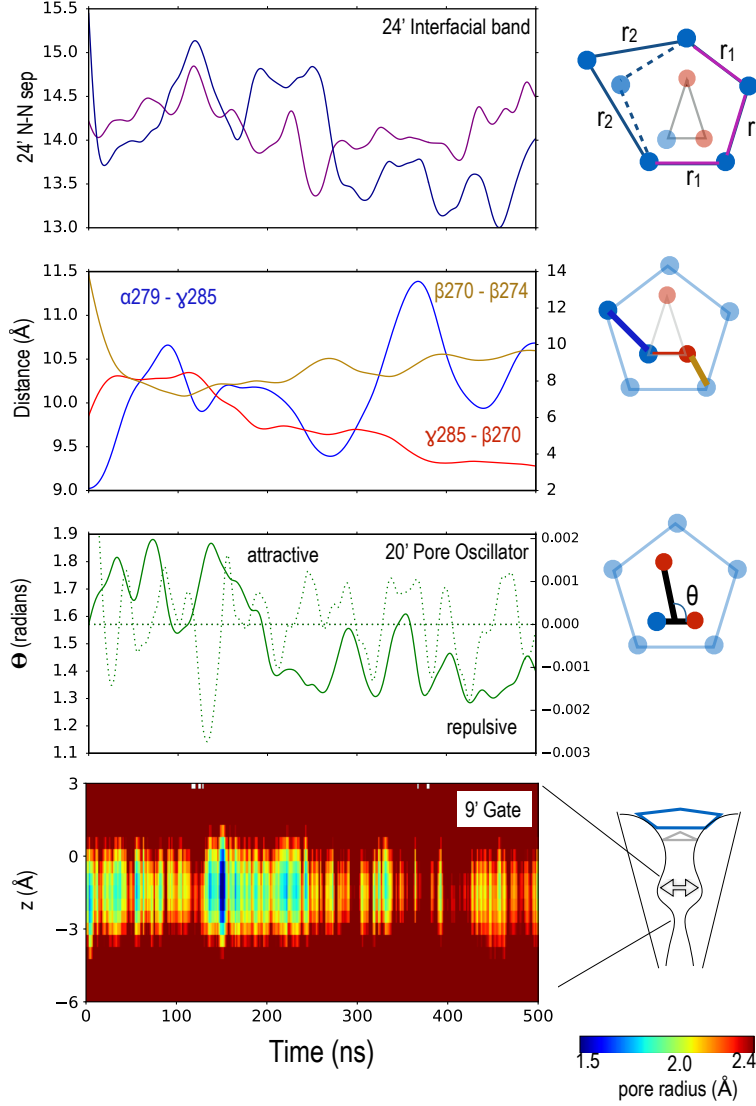
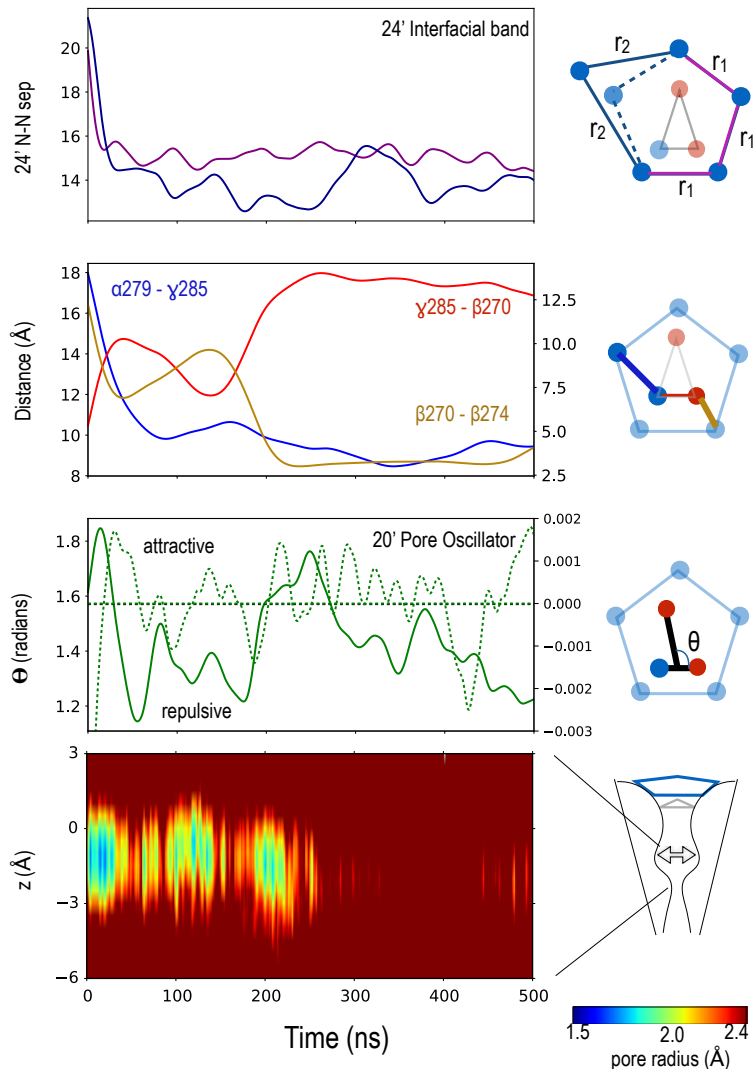


**Fig. S7. Evolution of the interfacial band and pore oscillator in one replica of the WT system at 315K.** (A) Residue ( $\alpha$ -K279) remains flipped from 300K simulations so the interfacial band remains in a regular pentamer form. (B) The distances between residues  $\alpha$ K279 –  $\gamma$ K285 –  $\beta$ -K270,  $\beta$ -K270 –  $\beta$ -K274, plotted on alternate y-axis, are shown in blue, red and gold respectively. (C) The solid green curve depicts the angle between the charge-dipole arrangement representing the pore oscillator ; The Dotted green line represents the pore-opening event as measured by calculating the first derivative of the minimum pore radii. (D) Pore radius as a function of distance along the pore axis and time. All curves are smoothed as described in SI Methods.

1117  
1118  
1119  
1120  
1121  
1122  
1123  
1124  
1125  
1126  
1127  
1128  
1129  
1130  
1131  
1132  
1133  
1134  
1135  
1136  
1137  
1138  
1139  
1140  
1141  
1142  
1143  
1144  
1145  
1146  
1147  
1148  
1149  
1150  
1151  
1152  
1153  
1154  
1155  
1156  
1157  
1158  
1159  
1160  
1161  
1162  
1163  
1164  
1165  
1166  
1167  
1168  
1169  
1170  
1171  
1172  
1173  
1174  
1175  
1176  
1177  
1178

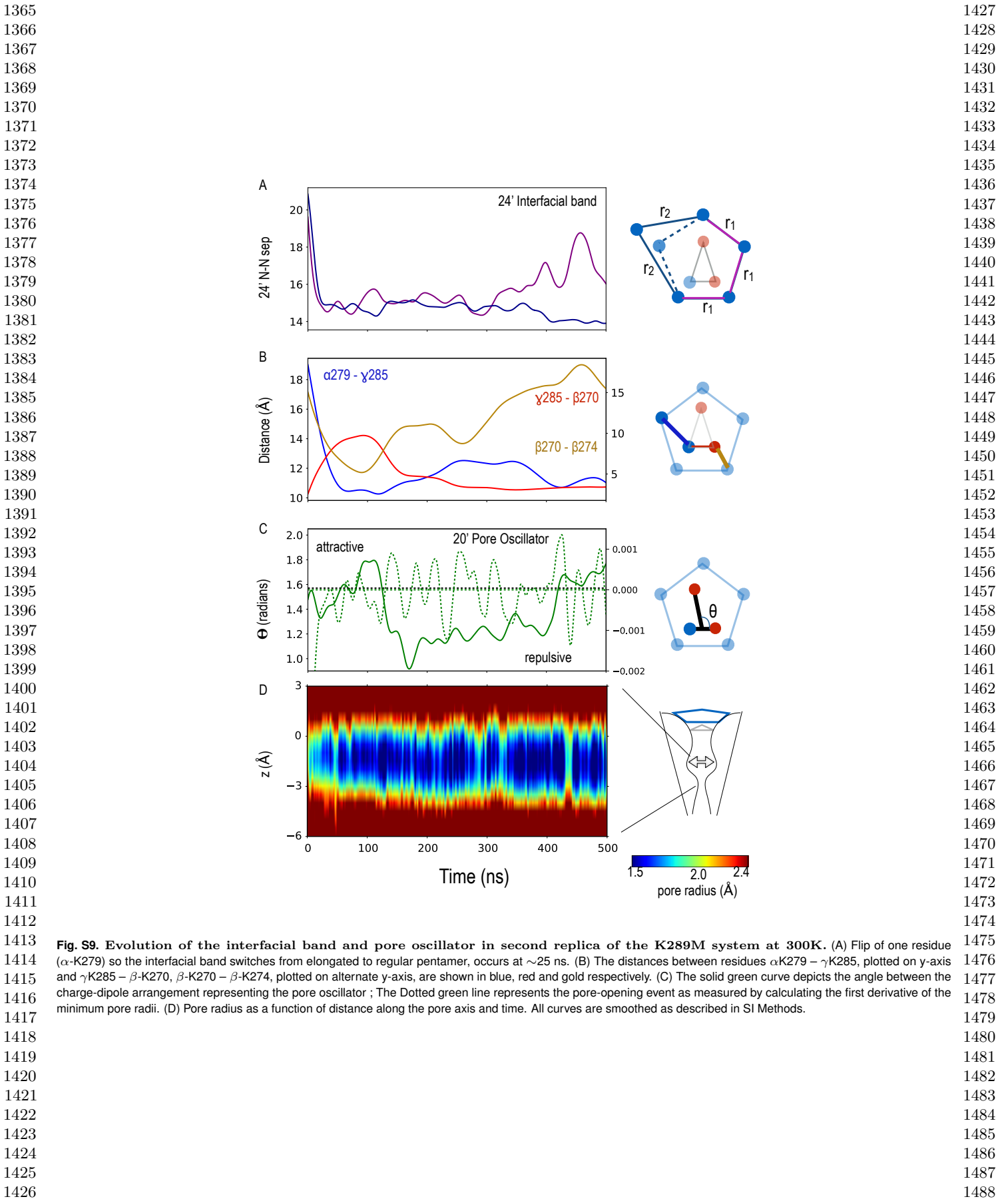
1179  
1180  
1181  
1182  
1183  
1184  
1185  
1186  
1187  
1188  
1189  
1190  
1191  
1192  
1193  
1194  
1195  
1196  
1197  
1198  
1199  
1200  
1201  
1202  
1203  
1204  
1205  
1206  
1207  
1208  
1209  
1210  
1211  
1212  
1213  
1214  
1215  
1216  
1217  
1218  
1219  
1220  
1221  
1222  
1223  
1224  
1225  
1226  
1227  
1228  
1229  
1230  
1231  
1232  
1233  
1234  
1235  
1236  
1237  
1238  
1239  
1240

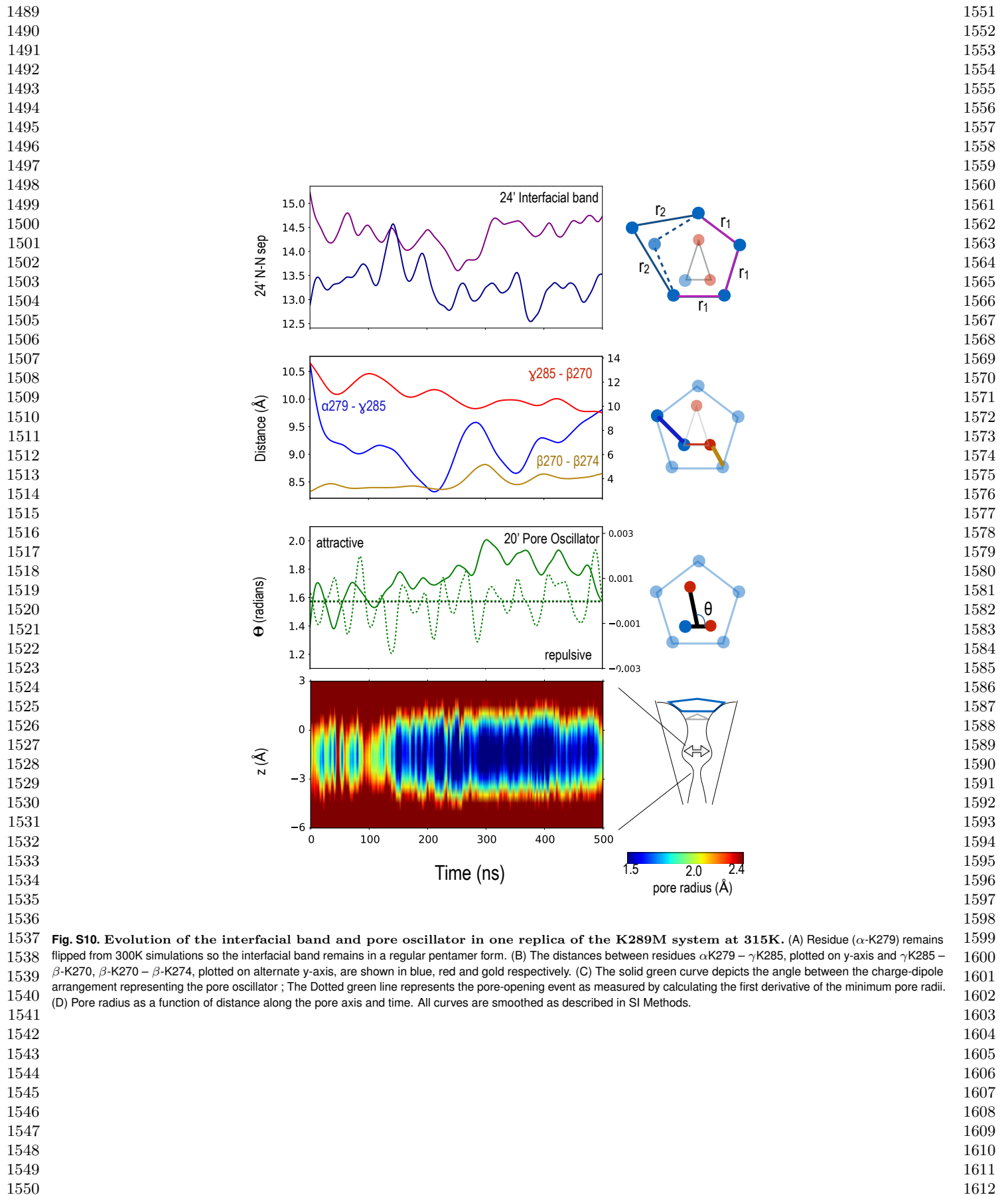
1241  
 1242  
 1243  
 1244  
 1245  
 1246  
 1247  
 1248  
 1249  
 1250  
 1251  
 1252  
 1253  
 1254  
 1255  
 1256  
 1257  
 1258  
 1259  
 1260  
 1261  
 1262  
 1263  
 1264  
 1265  
 1266  
 1267  
 1268  
 1269  
 1270  
 1271  
 1272  
 1273  
 1274  
 1275  
 1276  
 1277  
 1278  
 1279  
 1280  
 1281  
 1282  
 1283  
 1284  
 1285  
 1286  
 1287  
 1288  
 1289  
 1290  
 1291  
 1292  
 1293  
 1294  
 1295  
 1296  
 1297  
 1298  
 1299  
 1300  
 1301  
 1302

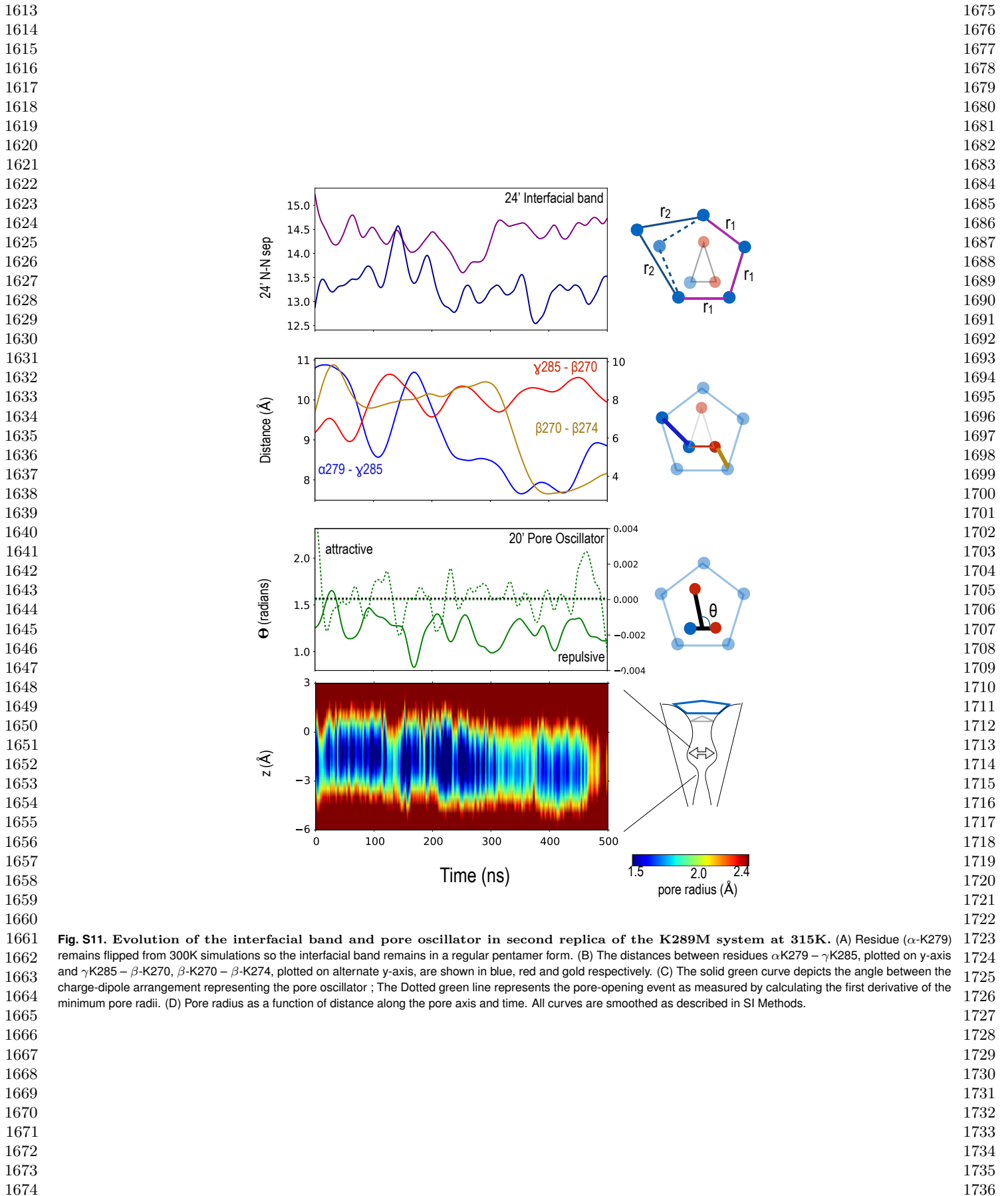


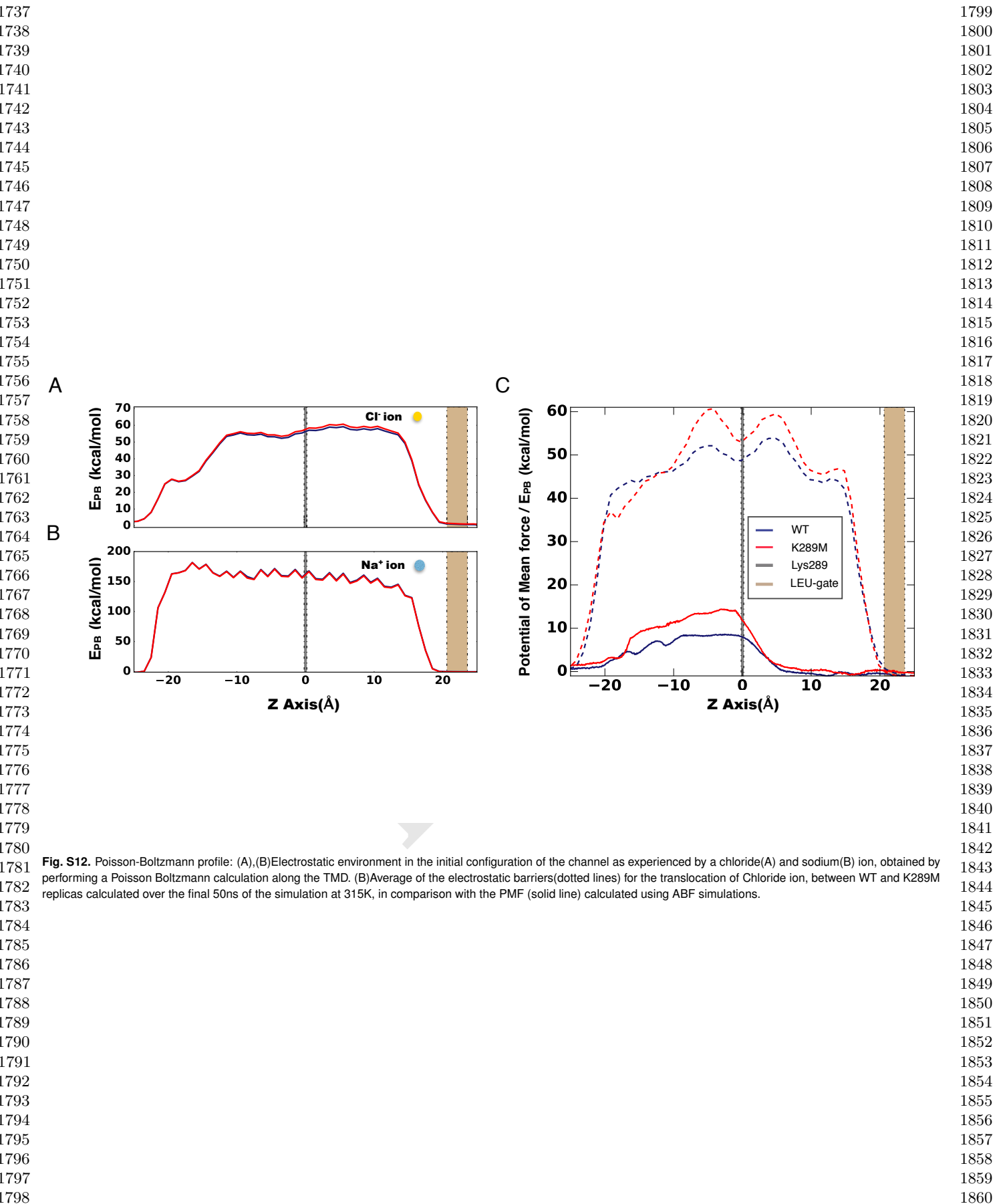
**Fig. S8.** Evolution of the interfacial band and pore oscillator in one replica of the K289M system at 300K. (A) Flip of one residue ( $\alpha$ -K279) so the interfacial band switches from elongated to regular pentamer, occurs at  $\sim 25$  ns. (B) The distances between residues  $\alpha$ -K279 –  $\gamma$ -K285,  $\beta$ -K270 –  $\beta$ -K274,  $\gamma$ -K285 –  $\beta$ -K270, plotted on alternate y-axis, are shown in blue, red and gold respectively. (C) The solid green curve depicts the angle between the charge-dipole arrangement representing the pore oscillator ; The Dotted green line represents the pore-opening event as measured by calculating the first derivative of the minimum pore radii. (D) Pore radius as a function of distance along the pore axis and time. All curves are smoothed as described in SI Methods.

1303  
 1304  
 1305  
 1306  
 1307  
 1308  
 1309  
 1310  
 1311  
 1312  
 1313  
 1314  
 1315  
 1316  
 1317  
 1318  
 1319  
 1320  
 1321  
 1322  
 1323  
 1324  
 1325  
 1326  
 1327  
 1328  
 1329  
 1330  
 1331  
 1332  
 1333  
 1334  
 1335  
 1336  
 1337  
 1338  
 1339  
 1340  
 1341  
 1342  
 1343  
 1344  
 1345  
 1346  
 1347  
 1348  
 1349  
 1350  
 1351  
 1352  
 1353  
 1354  
 1355  
 1356  
 1357  
 1358  
 1359  
 1360  
 1361  
 1362  
 1363  
 1364









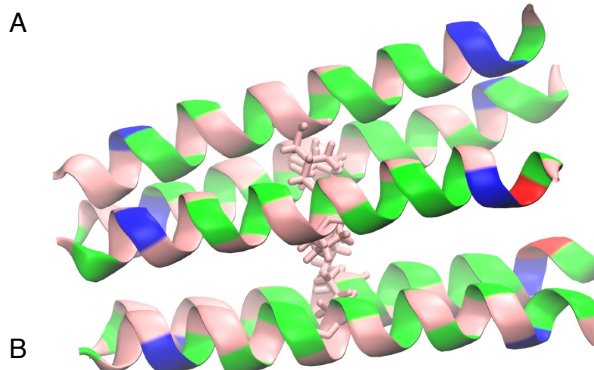


**Fig. S13.** (A) Snap-shot depicting the M2-helices (laid horizontally) showing the minimum constriction region flanked by LEU residues.(B) The force experienced by the ion as a function of position in the channel along the Z axis(TM domain), calculated by performing SMD on a Chloride passing along the pore of the channel.

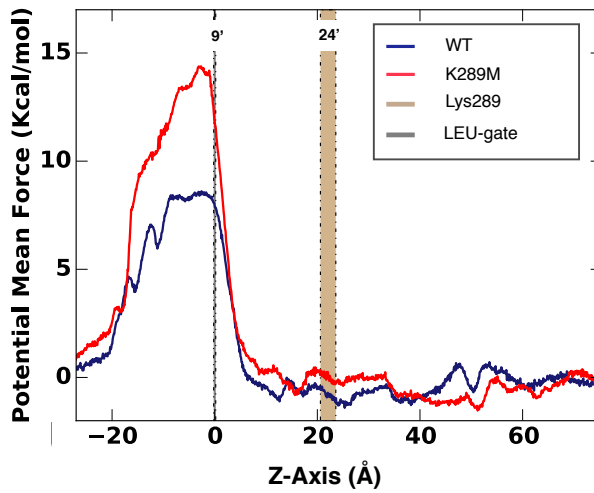


**Fig. S14.** (A) Potential of mean force profile of a chloride ion crossing the ion channel, calculated at 315K.

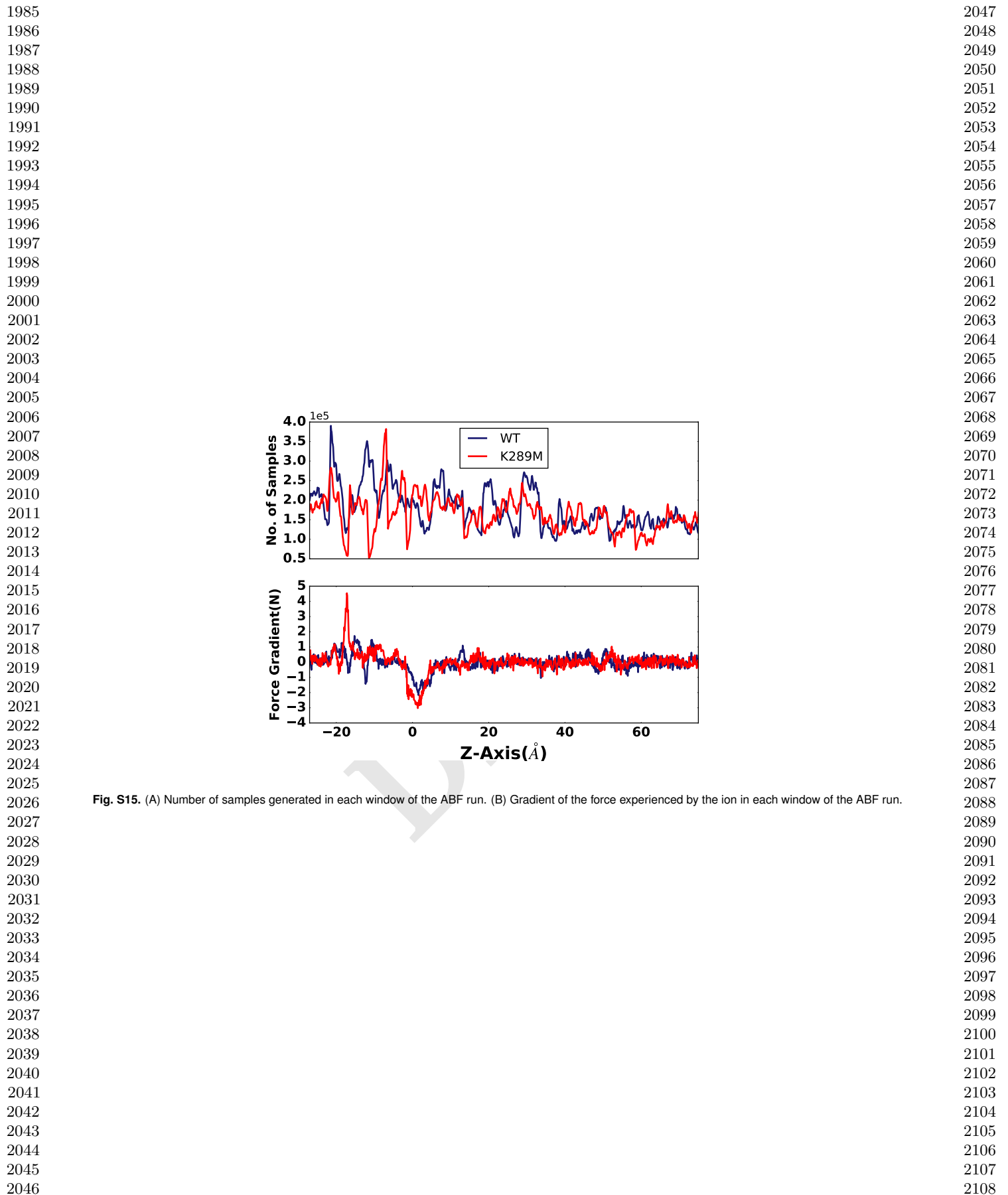


**Fig. S15.** (A) Number of samples generated in each window of the ABF run. (B) Gradient of the force experienced by the ion in each window of the ABF run.

2109	1. Humphrey W, Dalke A, Schulten K (1996) VMD: visual molecular dynamics. <i>Journal of molecular graphics</i> 14(1):33–8, 27–8.	2171
2110	2. Lev B, et al. (2017) String method solution of the gating pathways for a pentameric ligand-gated ion channel. <i>Proceedings of the National Academy of Sciences</i> 114(21):E4158–E4167.	2172
2111	3. Isralewitz B, Baudry J, Gullingsrud J, Kosztin D, Schulten K (2001) Steered molecular dynamics investigations of protein function. <i>Journal of Molecular Graphics and Modelling</i> 19(00):13–25.	2173
2112	4. Park S, Schulten K (2004) Calculating potentials of mean force from steered molecular dynamics simulations. <i>Journal of Chemical Physics</i> 120(2004):5946–5961.	2174
2113	5. Jarzynski C (1997) Nonequilibrium Equality for Free Energy Differences. <i>Physical Review Letters</i> 78(14):2690–2693.	2175
2114	6. Jarzynski C (1997) Equilibrium free-energy differences from nonequilibrium measurements: A master-equation approach. <i>Physical Review E</i> 56(5):5018–5035.	2176
2115	7. Hénin J, Chipot C (2004) Overcoming free energy barriers using unconstrained molecular dynamics simulations. <i>The Journal of chemical physics</i> 121(7):2904–14.	2177
2116	8. Darve E, Rodríguez-Gómez D, Pohorille A (2008) Adaptive biasing force method for scalar and vector free energy calculations. <i>The Journal of chemical physics</i> 128(14):144120.	2178
2117	9. Pohorille A, Jarzynski C, Chipot C (2010) Good practices in free-energy calculations. <i>J Phys Chem B</i> 114(32):10235–10253.	2179
2118	10. Comer J, et al. (2014) The Adaptive Biasing Force Method: Everything You Always Wanted to Know, but Were Afraid to Ask. <i>The journal of physical chemistry. B.</i>	2180
2119	11. Fiorin G, Klein ML, Hénin J (2013) Using collective variables to drive molecular dynamics simulations. <i>Molecular Physics</i> 111(22–23):3345–3362.	2181
2120	12. Smart OS, Nedubelil JG, Wang X, Wallace BA, Sansom MS (1996) HOLE: a program for the analysis of the pore dimensions of ion channel structural models. <i>J Mol Graph</i> 14(6):354–360,376.	2182
2121	13. Callenberg KM, et al. (2010) APBSmem: A graphical interface for electrostatic calculations at the membrane. <i>PLoS ONE</i> 5(9).	2183
2122	14. Dolinsky TJ, et al. (2007) PDB2PQR: expanding and upgrading automated preparation of biomolecular structures for molecular simulations. <i>Nucleic acids research</i> 35(Web Server issue):W522–5.	2184
2123		2185
2124		2186
2125		2187
2126		2188
2127		2189
2128		2190
2129		2191
2130		2192
2131		2193
2132		2194
2133		2195
2134		2196
2135		2197
2136		2198
2137		2199
2138		2200
2139		2201
2140		2202
2141		2203
2142		2204
2143		2205
2144		2206
2145		2207
2146		2208
2147		2209
2148		2210
2149		2211
2150		2212
2151		2213
2152		2214
2153		2215
2154		2216
2155		2217
2156		2218
2157		2219
2158		2220
2159		2221
2160		2222
2161		2223
2162		2224
2163		2225
2164		2226
2165		2227
2166		2228
2167		2229
2168		2230
2169		2231
2170		2232